JMEPEG (2018) 27:4261–4269
https://doi.org/10.1007/s11665-018-3487-3

1059-9495/$19.00

Microstructural Characterization and High Strain Rate Plastic Flow Behavior of SMAW Armox500T Steel Joints from Spherical Indentation Experiments

Ambuj Saxena, A. Kumaraswamy, Sanghamitra Sethi, G. Madhusudhan Reddy, and Vemuri Madhu

(Submitted September 6, 2017; in revised form February 27, 2018; published online July 5, 2018)

Static indentation and uniaxial compression tests have been conducted on Armox500T steel and its weldments to predict the constraint factor (CF), i.e., ratio of Meyer's hardness to uniaxial flow stress. Series of dynamic indentation experiments were carried out at impact velocities ranging from 5 to 300 m/s to estimate dynamic hardness as a function of average strain. Subsequently, dynamic indentation (DI) test data and CF determined under static indentation conditions have been used to study the high strain rate plastic flow behavior of Armox500T weldments in comparison with the base metal. It was observed that flow stress for Armox500T and its weldments under dynamic loading conditions (10^4 s^{-1}) are significantly higher than flow stress measured under static loading conditions (10^{-3} s^{-1}). The plastic flow behavior computed from DI is in good agreement with the data evaluated through conventional split Hopkinson pressure bar technique. Further, the study of the microstructure of base metal and weldments by optical microscopy and SEM revealed a considerable variation in the microstructure.

Keywords Armox500T weldments, constraint factor, plastic flow behavior, SEM, SHPB, spherical indentation

1. Introduction

Armor steels are widely used in building civil and military structures such as battle tanks, armored vehicles, helicopter components for improved reliability, durability, weldability, the safety of structures, equipment and extended machinery or constructions working life. Tempered Armox500T steel possesses ultra-high strength and high hardness to resist penetration against projectiles (Ref 1). The primary requirement of the military structure is to minimize the mass and volume without compromising on necessary mechanical and ballistic properties. Turret and hulls in combat vehicles, landing gears, earth moving, mining equipment and mortar casings made of Armox500T are commonly fabricated by shielded metal arc welding (SMAW). The SMAW with low hydrogen ferrite (LHF) and austenitic stainless steel (ASS) welding consumables are commonly used to prevent hydrogen-induced cracking (HIC), as they have higher solubility for hydrogen in the austenitic phase. Further, ASS consumable as filler metal is used in welding of heavy structures in shipbuilding, pressure vessels and heavy vehicles to obtain good impact properties along with adequate strength. All the above applications involve ballistic impact, collision, detonation, shaped charge threats, etc. Under these circumstances, the welded mechanical structures are subjected to high loading rates and experience large plastic strains of the order of 10^2-10^4 s^{-1}. Further, welding consumables and welding processes have a considerable effect on the performance of quenched and tempered steel joints, especially in impact applications. To analyze these phenomena, the rate dependence of mechanical properties of welding consumables employed needs to be fully characterized.

High-velocity impact problems are associated with constrained deformations unlike deformations existing in uniaxial tensile or compression tests. The conventional high strain rate techniques such as SHPB, Taylor cylinder techniques, pressure shear plate impact determine flow behavior under unconstrained conditions (Ref 2). Further, the equipment and instrumentation required to generate the data to obtain the flow behavior are quite sophisticated. The constrained deformation behavior of metals and alloys at high strain rates (10^2-10^4 s^{-1}) was studied by DI technique (Ref 2-7). In general, it is assumed that Tabor relationship for average strain and CF determined from static indentation tests are valid under DI conditions too (Ref 8, 9). Numerous researchers have investigated the effect of CF on deformation behavior under static indentation conditions (Ref 10-14). The CF for ductile crystalline solids was found to be in the range of 2.4-3.0 (Ref 13, 14) and above 3.0 in case of pressure sensitive materials like metallic glass (Ref 15). Majority of the earlier researchers analyzed steels, Cu and Al alloys at room temperature (Ref 10-12) and Kumaraswamy et al. (Ref 13, 14) have studied the temperature dependence on CF of Ti64 and IN718. It clearly points to the fact that data on the plastic flow behavior of multi-pass SMAW Armox 500T joints fabricated by ASS and LHF welding consumables under dynamic loading conditions in comparison with base metal are seldom available in the published literature.

In view of the above, in the present work, an attempt has been made to predict the constraint factor from static indentation and compression tests. Subsequently, the effect of welding consumables on the high strain rate (10^4 s^{-1}) plastic flow behavior of Armox500T steel weldments in comparison

Ambuj Saxena and **A. Kumaraswamy**, Department of Mechanical Engineering, Defence Institute of Advanced Technology (DIAT), Girinagar, Pune 411025, India; and **Sanghamitra Sethi**, Marathwada Mitra Mandal's College of Engineering, Pune 411025, India; and **G. Madhusudhan Reddy** and **Vemuri Madhu**, Defence Metallurgical Research Laboratory, Kanchanbagh, Hyderabad 500048, India. Contact e-mails: akswamy@diat.ac.in, adepu_kswamy@yahoo.com.

with base metal has been evaluated through DI experiments. The results have been compared with the data generated through split Hopkinson pressure bar (SHPB) experiments. In the end, A few deal of research has been focused on the microstructural characterization of Armox500T steel and its weldments.

2. Experimental Details

2.1 Welding of Armox500T Plates

As received, Armox500T steel was water quenched from 1273 K and tempered in the range of temperatures 473-773 K. Prior to quenching and tempering the steel was hot rolled at 1523 K. Armox500T plates were joined by shielded metal arc welding (SMAW) using two different electrodes, i.e., austenitic stainless steel (ASS) and low hydrogen ferritic (LHF) steel consumable as shown in Fig. 1(a). The parameters considered in SMA welding are given in Table 1. Compression, static and dynamic indentation, and SHPB samples have been wire cut from the Armox500T plate in rolling direction (hereafter referred to as base metal) and fusion zone of two weldments in the configuration shown in Fig. 1(b). Weldments produced by LHF steel electrode and ASS electrode are referred to as weldment-1 and weldment-2, respectively. Top and bottom surfaces of all the test samples were carefully ground and polished to maintain flatness and parallelism within ± 1 μm. To ensure the repeatability, three samples were tested for a given condition.

2.2 Compression Test

Compression tests were carried out on base metal and weldment samples as per standard test procedure. Test setup, sample dimensions and strain rate considered are given in Table 2. Load versus compression data was converted to true stress–strain and subsequently true stress–true plastic strain by removing the elastic component of strain (Ref 13, 14). MoS_2 layer of 100 μm thick was used as a lubricant to minimize friction at platen/specimen interface.

2.3 Static Indentation Test

Static indentation test was carried out on base metal and weldment samples as per standard test procedure. Test setup, load range, indenter and sample dimensions considered are given in Table 2. The hardness of WC ball (2020 HV) was five times higher than the test materials under investigation. The load received by the test specimen during indentation was measured by a load cell to an accuracy of ± 1 N. Further, the diameter of the residual impressions and lip height or pileup around indentation at different loads was measured from crater profiles. The contours of crater profiles from static indentation of base metal are shown in Fig. 2. The Meyer's hardness H_M, based on the projected area of the crater, and the average strain ε_{av} experienced by the specimen during the indentation comparable to true plastic strain in uniaxial compression were then calculated (Ref 13, 14).

2.4 Dynamic Indentation Test

High-velocity gas gun (HVGG) capable of driving the spherical ball projectile at different impact velocities normal to target surface used for DI tests was developed at DIAT, Pune. The variation of impact velocity of the projectile was obtained by varying the gas pressure. The range of velocity, strain rate, projectile and sample dimensions are given in Table 2. H_d versus ε_{av} behavior was obtained from DI tests conducted on a number of test samples (base metal and weldments) as described below. WC ball projectile was impacted on test sample rigidly held in a specially designed massive fixture. The dimensions of the residual impressions formed due to ball impact and lip height around indentation at different velocities were measured from crater profiles to an accuracy of ± 1 μm. The contours of crater profiles from DI of base metal are shown in Fig. 3. Average strain ε_{av} experienced by the test specimen, dynamic hardness H_d in MPa and average strain rate ε' associated with each data point were determined (Ref 4, 7).

Table 1 SMA welding process parameters

Parameters	Weldment-1	Weldment-2
Electrode	E 7018 ((LHF)	E 308 (ASS)
Electrode diameter, mm	4	4
No. of passes	5	5
Welding speed, mm/min	130	130
Arc voltage, V	18-20	26-28
Welding current, A	110	100
Arc gap, mm	2	2
Heat input, kJ/mm	1.01	1.29

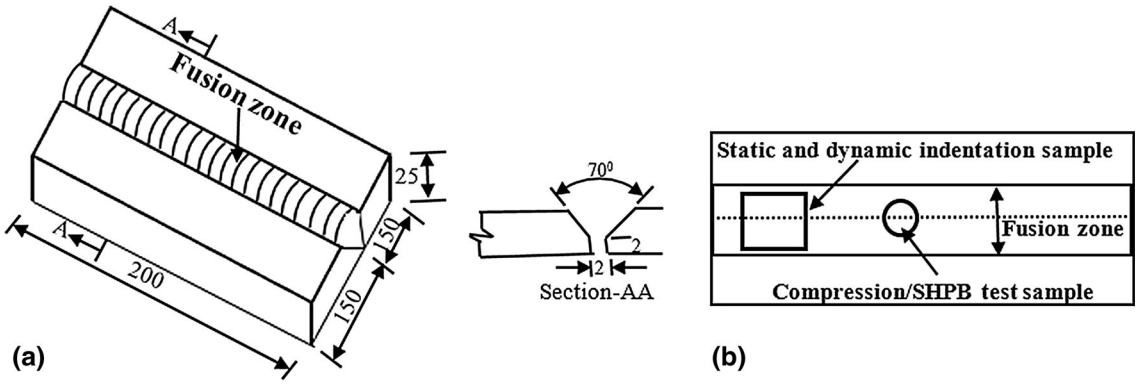

Fig. 1 (a) Schematic of SMAW joint and (b) test samples wire cut from fusion zone

Table 2 Mechanical test parameters

Mechanical test	Test setup	Load/velocity range	Sample dimensions, mm	Strain rate, s^{-1}
Compression	Computer-controlled Walter + Bai Ag UTM	0-98 kN	ϕ 5 × 10	10^{-3}
Static indentation (ϕ 10 WC ball indenter)	Computer-controlled Brinnel hardness tester	5-50 kN	20 × 25 × 12.5	10^{-3}
Dynamic indentation (ϕ 4.76 WC ball projectile)	High-velocity gas gun (HVGG)	5-300 m/s	20 × 25 × 12.5	10^{4}
SHPB compression	SHPB setup	10-45 m/s	ϕ 6 × 3	10^{4}

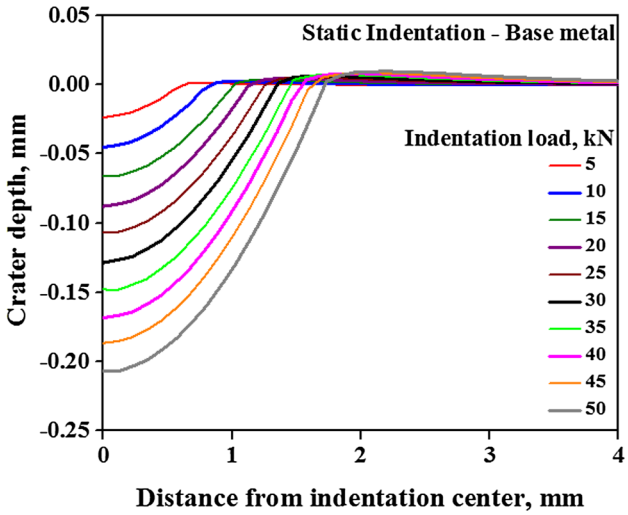

Fig. 2 Crater profiles of residual impressions produced from static indentation

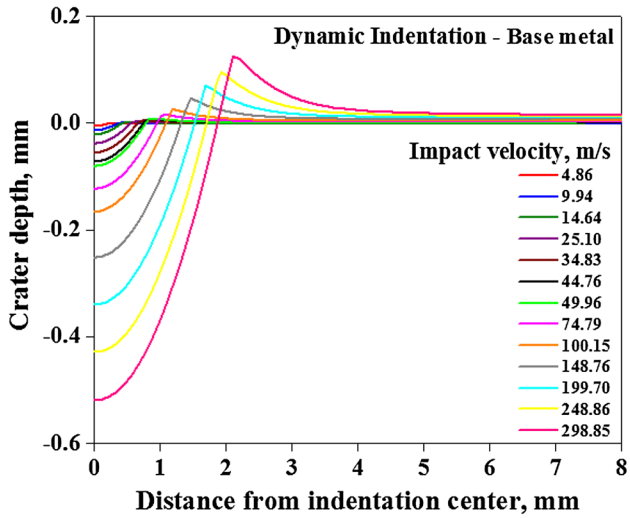

Fig. 3 Crater profiles of residual impressions produced from dynamic indentation

2.5 Dynamic Compression Test

Conventional dynamic compression tests were conducted on SHPB test setup consisting of striker, incident and transmitted bars as shown in Fig. 4 (Ref 16). The cylindrical sample is held between the incident and transmitted bars which are fitted with strain gauges during the test. The striker bar is impacted on the incident bar to form a trapezoidal incident stress impulse wave that will travel through the incident bar and the specimen in the axial direction. The portion of this pulse is transmitted through the sample to the transmitted bar, while the balance is reflected back to the incident bar due to material mismatch. The amplitude of the incident pulse is directly proportional to impact velocity. Further, increase in incident pulse affects the transmitted and reflected pulse, which in turn influences the strain rate. The range of velocity, strain rate considered and sample dimensions are given in Table 2. The true stress–true strain and strain rate of the test materials (base metal and weldments) were determined with one-dimensional assumption (Ref 17).

2.6 Microstructural Characterization

The standard metallographic technique was used to prepare the sample for microstructural characterization of base metal and weldments as described below:

- A solution made of 1 gm picric acid, 5 mL HCl, and 100 mL ethanol was used for etching of base metal.
- 3% Nital (3% nitric acid in ethanol) was used for etching of weldment-1 processed by low hydrogen ferrite (LHF) electrode. The sample was immersed in pure water and subsequently dried using pressured N_2 gas blowing.
- A solution made of 30 ml HCl, 15 ml HNO_3 and 5% HF was used for etching of weldment-2 processed by ASS electrode.

Optical microstructures and backscattered SEM images were taken from the semi-automatic microscope (Leica Microsystems) and SEM Σigma (Zeiss, beam step size 30 μm), respectively.

3. Results and Discussion

3.1 Microstructural Observations

The backscattered SEM image and an optical micrograph of the base metal, weldment-1 and weldment-2 are shown in Fig. 5, 6, and 7, respectively. The chemical composition (wt.%) determined by EDX method is given in Table 3. The detailed microstructural observations from SEM and optical microscope are given in the following sections.

3.1.1 Armox500T Steel (Base Metal). Backscattered SEM image of Armox500T steel shown in Fig. 5(a) indicates tempered martensite lath in acicular form with coarse and fine precipitate along with some grain boundaries. The optical micrograph is shown in Fig. 5(b) indicates the presence of columnar and blocks of laths. It is known that mechanical properties are structure sensitive (Ref 18, 19), they vary with

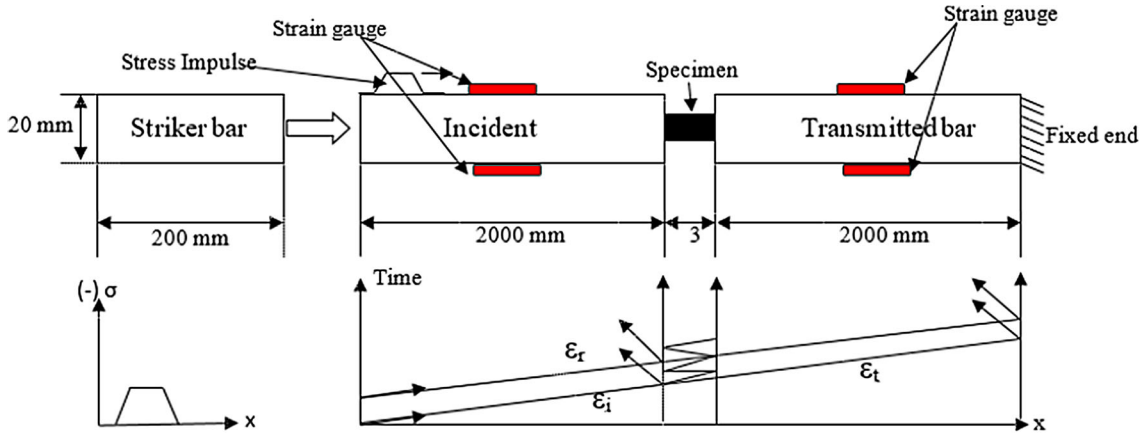

Fig. 4 Schematic of incident, reflected, and transmitted waves in SHPB

the amount and distribution of phases like retained austenite with martensite. Therefore, micrographs with higher magnification were used for closer identification of precipitation. The tendency of cracking is reduced with the increased amount of retained austenite, which is transformed to martensite as observed in parent materials. Further, an optical micrograph is showing white etching wedge-shaped Widmanstätten ferrite plates in a matrix quenched to martensite. These plates are coarse and etch containing very little substructure that is evident through strain hardening and uniform strain distribution.

3.1.2 Weldment-1 (Processed with LHF Electrode). Backscattered SEM image and an optical micrograph of weldment-1 shown in Fig. 6 indicate micro-cracks without any voids evidencing sound and clear welding joint. Nucleation and growth tendencies are influenced by chilling action of the parent metal that gives dendritic grain size within the weld. The microstructure of weldment-1 is mainly acicular ferrite associated with second phase containing Widmanstätten and Bainite phase without martensite (Ref 20-23). This type of microstructure containing large colony size and oriented laths is undesirable in welding because it offers little resistance to crack propagation (Ref 24-27). Further, these phases cannot migrate to the grain boundaries and hence separated inside the grains. In addition, the acicular ferrite microstructure also consists of small particles of intergranularly nucleated ferrite without any particular orientation. Thus, the resulting small effective grain size and lack of orientation make acicular ferrite a desirable weld microstructure with excellent mechanical properties compared to weldment-2 as described in the following section.

3.1.3 Weldment-2 (Processed with ASS Electrode). Backscattered SEM image and an optical micrograph of weldment-2 shown in Fig. 7 are mainly composed of austenite and partial δ-ferrite phase. In general, coarse-grained or mixed grain size structure obtained by fast heating and cooling in the weld region causes the properties of the weld region to be completely different from the properties of the parent metal. In addition, residual stresses are developed in the weld region due to high hardness martensite formation resulting from rapid cooling of the weld zone. As the temperature decreases, the grain size changes from coarse to fine. Hence, it is suggested to do annealing for stress-relieving and recrystallization to increase the life of weld region (Ref 24, 28-30). The amount of δ-ferrite was estimated using Cr and Ni equivalents of weld metal chemical composition (Ref 28). Cr and Ni equivalents are found to be 18.8 and 11.5, respectively, and about 5 (vol.%) ferrite was existing in the austenitic matrix based on the Schaeffler diagram (Ref 28) shown in Fig. 8.

3.2 Compressive Flow Behavior

Compression tests were carried out for base metal and weldments as described under "section 2.2" to obtain true stress versus plastic strain (σ–ε) behavior (Ref 13, 14). The flow stress increased with increase in plastic strain indicating strain hardening of the test samples as shown in Fig. 9. σ–ε plots obtained were fitted to *Holloman* constitutive equation, $\sigma = K\varepsilon^n$, and best-fit values of n and K are listed in Table 4. The flow stress of weldment-1 and weldment-2 at 7% strain was observed to be 33 and 29% of its base metal, respectively, indicating the influence of electrode used in welding process on mechanical properties of the test materials.

3.3 Meyer's Hardness Behavior

Static indentation tests have been carried out for base metal and weldments as explained under "section 2.3" to obtain $H_M - \varepsilon_{av}$ behavior as shown in Fig. 10. The Meyer's hardness increased with increase in average strain due to strain hardening during indentation. $H_M - \varepsilon_{av}$ plots were curve fitted to *Holloman* power law, $H_M = A\varepsilon_{av}^p$. The best-fit values of indentation strain-hardening exponent p and strength coefficient A obtained from experiments are mentioned in Table 4. The H_M value of weldment-1 and weldment-2 at a given strain, say 7% average strain, was found to be 27 and 20% of its base metal, respectively, indicating the effect of electrode used in welding process on properties of the test materials under static indentation conditions.

3.4 Estimation of Constraint Factor

The factor by which the resistance to plastic flow underneath indenter is greater than uniaxial flow stress is considered as constraint factor (CF). The ratio of Meyer's hardness to flow stress at a given strain essentially gives the value of CF. The CF values for base metal and weldments were determined at

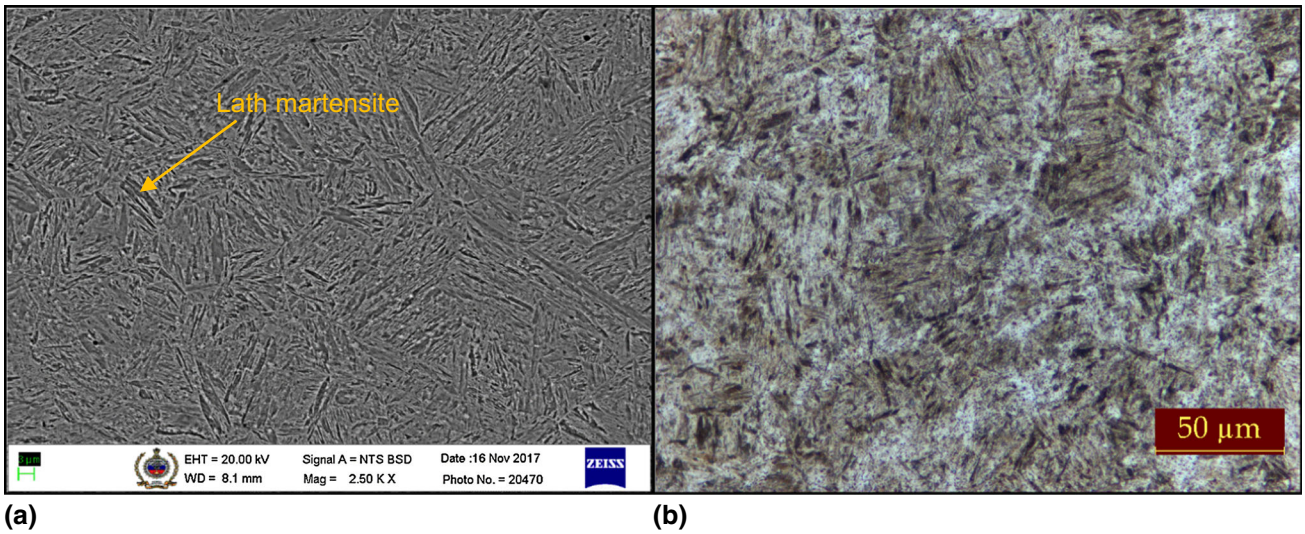

Fig. 5 Armox500T base metal (a) back scattered SEM and (b) optical micrograph

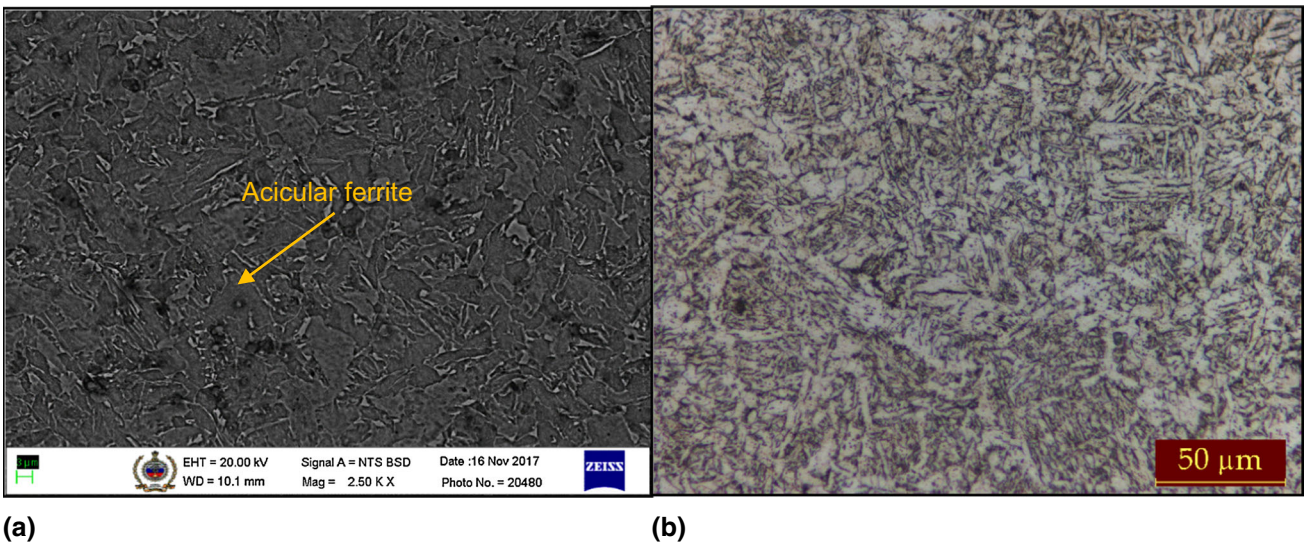

Fig. 6 Weldment-1 (a) back scattered SEM and (b) optical micrograph

different strains using $H_M - \varepsilon_{av}$ and σ–ε data plotted on a common scale. The CF value increased with increase in strain up to certain strain called transition strain ε_{tr}, after which the value was observed to be independent of strain as shown in Fig. 11. The transition occurred at 5.81, 9.44 and 9.71% strain, and CF value in the fully plastic regime was 2.93, 2.77 and 2.67 for base metal, weldment-1 and weldment-2, respectively. Tirupataiah et al. (Ref 10-12) and Kumaraswamy et al. (Ref 13, 14) have reported that CF value for pure metals was around 2.4, and alloys was in the range of 2.6-3.0. In the elastic–plastic regime, the strain-hardening ability n has a distinct effect on CF, i.e., lower the value of n higher will be CF. In the present study, base metal has a lower value of n (0.042) and higher CF (2.93) compared to weldments indicating good agreement with the literature data. Most of the previous studies on CF involved Cu, Al alloys, steels, Ti-6Al-4V and IN718. Therefore, the data on CF for Armox500T weldments in comparison with base metal from the current study report for the first time.

The CF determined under static indentation conditions is applicable for DI too due to quasi-static nature of the deformation during dynamic indentation (Ref 4, 7). To verify the applicability of CF at high strain rates, selective indentations obtained from static and DI of base metal and weldment samples at 6% strain were sectioned along their diameter and polished. Subsequently, microhardness (Knoop, 50 g load) normalized over base microhardness versus depth below indentation normalized over indentation diameter was evaluated. It was observed that microhardness profiles under static and DI conditions were similar indicating quasi-static condition during impact process.

3.5 High Strain Rate Plastic Flow Behavior

The $H_d - \varepsilon_{av}$ data for the base metal and weldments are plotted in Fig. 12. The dynamic hardness, H_d, increased gradually as a function of strain up to critical strain ε_c and

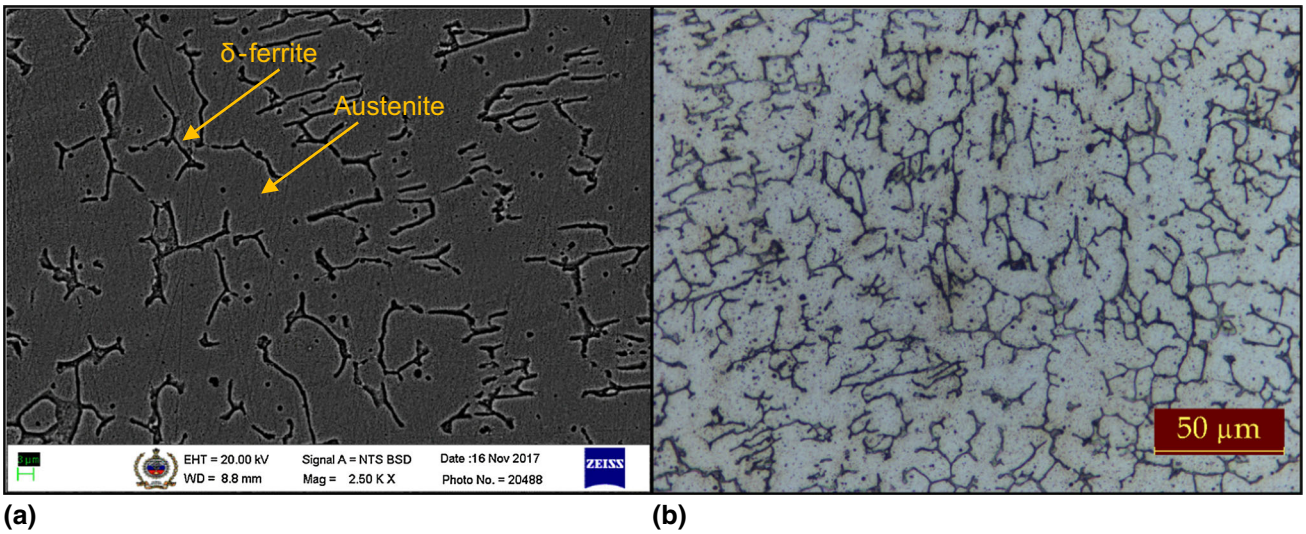

Fig. 7 Weldment-2 (a) back scattered SEM and (b) optical micrograph

Table 3 Chemical composition (wt.%) of test materials and welding electrode

Material	C	Si	Mn	P	S	Cr	Ni	Mo	N	B	Fe
Base metal	0.31	0.265	0.86	0.019	0.007	0.60	0.82	0.24	…	0.005	Balance
Weldment-1(a)	0.06	0.58	0.85	0.017	0.012	0.04	0.03	0.015	0.018	…	Balance
Weldment-2(b)	0.05	0.51	1.18	0.018	0.06	18.03	9.45	…	0.04	…	Balance

(a) E7018, (b) E308

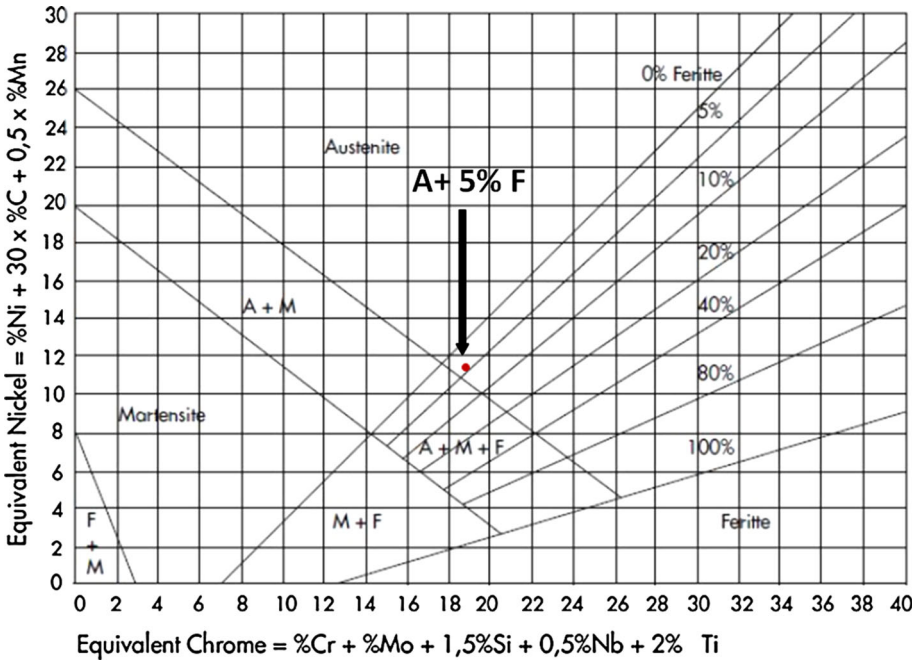

Fig. 8 Mapping of Austenite + δ-ferrite (18.8 Cr and 11.5 Ni) in Schaeffler diagram (weldment-2)

subsequently reduced with a further increase in strain. This is due to localization of plastic deformation after critical strain underneath the ball indenter. The severe concentration of strain in the narrow region causes substantial temperature rise and consequent thermal softening. As a result, the diameter of residual impression is greater than its value in the absence of

localization. A similar trend was observed in case of Cu, steels, Al alloys, Fe and Ti-6Al-4V (Ref 4, 7). $H_d - \varepsilon_{av}$ plots up to critical strain were curve fitted to the power law, $H_d = H_{od}\varepsilon_{av}^{n_d}$. The best-fit values of dynamic indentation strain-hardening exponent n_d and strength coefficient H_{od} obtained from experiments are mentioned in Table 4. The strain rate ε' pertinent to the current DI data is $(2.08 \pm 1.58) \times 10^4$, $(1.37 \pm 1.0) \times 10^4$ and $(1.24 \pm 0.89) \times 10^4$ s^{-1} for base metal, weldment-1 and weldment-2, respectively. This is around 6-7 orders of magnitude higher compared to indentation under static loading conditions. The H_d value for base metal, weldment-1 and weldment-2 at a given strain during hardening phase of DI is about 1.6, 1.8 and 1.9 times the hardness, respectively, under static loading conditions. This indicates that strain rate has a significant effect on weldments compared to its counterpart base metal. Further, it may be noted that localization of plastic deformation was onset earlier in weldment-1 and weldment-2 compared to its counterpart base metal as shown in Fig. 12.

$H_d - \varepsilon_{av}$ plots up to critical strain, and CF values in the fully plastic regime estimated from static indentation (Fig. 11) were used to evaluate flow stress σ_d under dynamic loading conditions. The ratio of H_d at different strains and CF (H_d/CF) for base metal, weldment-1 and weldment-2 essentially represent high strain rate plastic flow ($\sigma_d - \varepsilon_{av}$) behavior of test materials as shown in Fig. 13. It may be noted that σ_d representing resistance to plastic flow at high strain rates for weldment-2 processed by ASS consumable is higher than weldment-1 processed by LHF consumable in the range of strains considered in the present study. It is also observed that the σ_d value of base metal and its weldments are about 1.5-1.7 times the value of the flow stress under static loading conditions indicating the effect of strain rate on base metal and its weldments. Further, it can be seen from Fig. 13 that the σ_d of

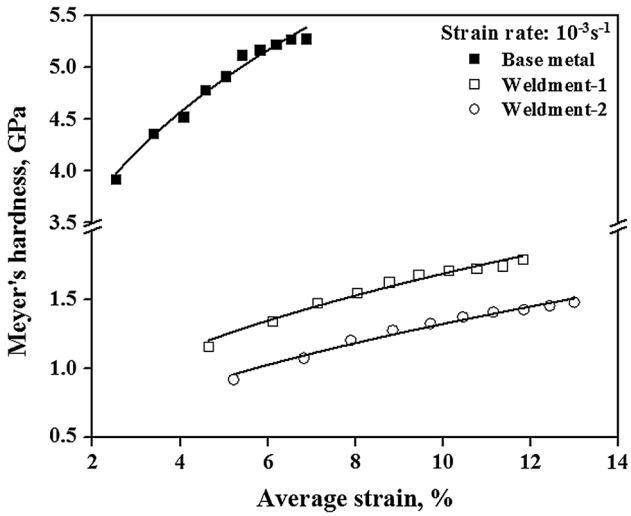

Fig. 10 Meyer's hardness vs. average strain

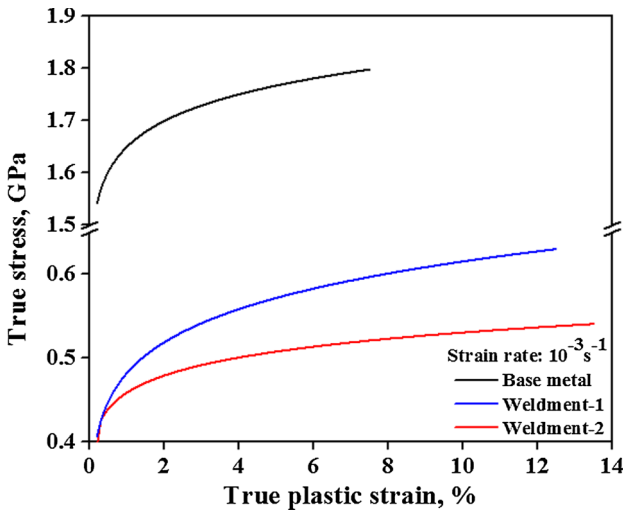

Fig. 9 Compressive flow stress vs. plastic strain

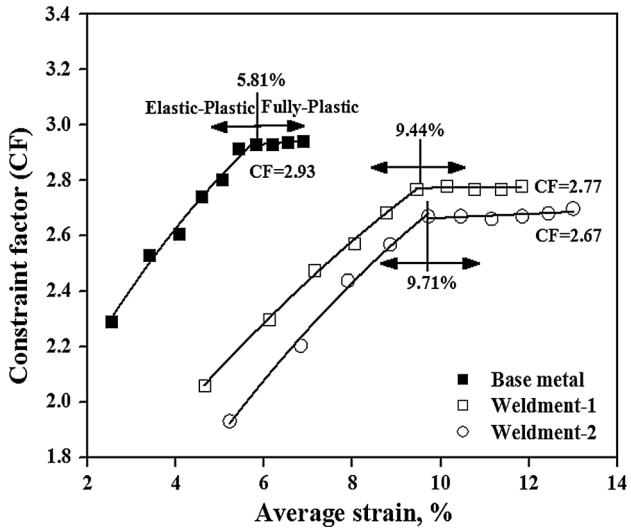

Fig. 11 CF vs. average strain

Table 4 Experimental properties of weldments/base metal under investigation

	Static indentation			Dynamic indentation				Compression test			
Material	Strain range, %	p	A, MPa	Strain range, %	H_{od}	n_d	Strain rate ($s^{-1} \times 10^4$)	Strain range, %	Yield stress, MPa	n	K, MPa
Base metal	2.50-6.90	0.30	2973	2.20-15.70	6381	0.15	2.08 ± 1.58	0.2-7.50	1523	0.042	1649
Weldment-1(a)	4.70-11.80	0.44	609	3.00-19.60	1745	0.21	1.37 ± 1.00	0.2-12.50	405	0.106	482
Weldment-2(b)	5.20-13.00	0.49	419	3.10-20.00	1359	0.20	1.24 ± 0.89	0.2-13.50	395	0.063	458

(a) E7018, (b) E308

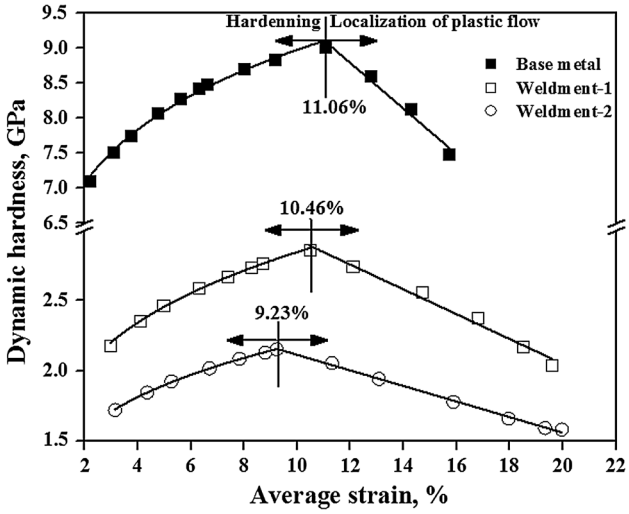

Fig. 12 Dynamic hardness vs. average strain

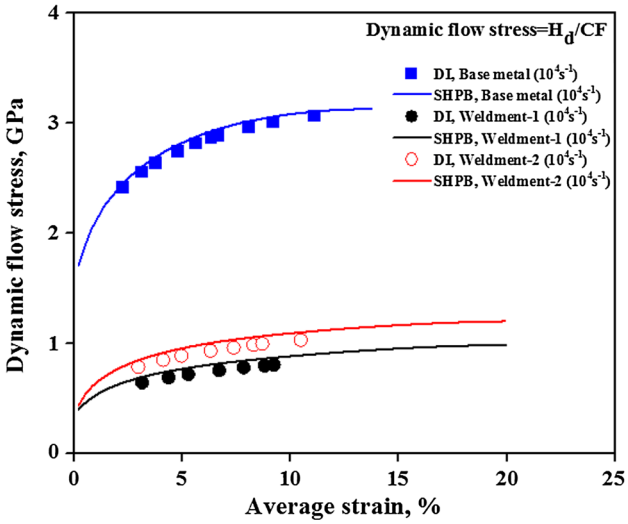

Fig. 13 Dynamic flow stress vs. average strain

all the test samples evaluated from DI is in good agreement with the data generated from SHPB tests at 10^4 s^{-1}.

The high strain rate plastic flow behavior of multi-pass SMA welded joints fabricated using LHF and ASS electrodes in comparison with its base metal reported in this study is first of its kind. In view of various high strain rate applications involving Armor steels highlighted earlier under introduction, the data generated in the current research assume utmost importance.

3.6 Pileup Around Indentation

The pileup around indentation obtained from static and DI was measured from the crater profiles as explained under "sections 2.3" and "2.4". The lip height h representing pileup increased marginally with strain under static loading and rapidly under DI conditions as shown in Fig. 14. This indicates that the effect of strain rate on upward flow of the material is predominant. Further, it may be noted that h value at a given strain for base metal is higher (low value of n) compared to weldments (high value of n) under static and DI conditions.

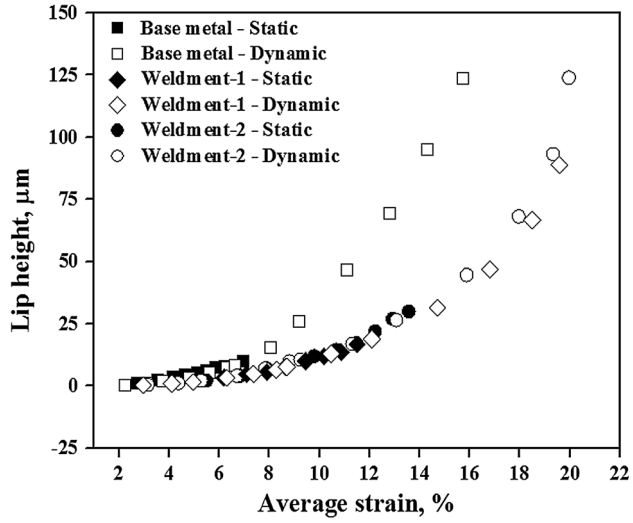

Fig. 14 Lip height vs. average strain

This is due to the fact that materials with high strain-hardening capability will accommodate more volume of the material displaced by indenter during static/dynamic indentation, thereby reducing the upward flow around the indentation (Ref 12-16).

4. Conclusions

1. SEM image of base metal mainly consists of tempered martensite lath in acicular form with coarse and fine precipitate along with some grain boundaries. The optical micrograph indicates the presence of columnar and blocks of laths.
2. The microstructure of weldment-1 mainly consists of acicular ferrite associated with second phase containing Widmanstätten and Bainite without martensite. Further, coarse grain changes to fine grain from maximum arc welding temperature to ambient temperature. On the other hand, the microstructure of weldment-2 mainly composed of austenite and partially δ-ferrite phase.
3. Flow stress and H_M values at a given strain say 7% for Armox500T weldments are approximately 29-33 and 20-27%, respectively, of its base metal, indicating that resistance to plastic flow of SMAW joints is significantly less compared to its base metal under static loading conditions.
4. CF value for weldment-1 (n = 0.106), weldment-2 (n = 0.063) and base metal (n = 0.042) is 2.77, 2.67 and 2.93, respectively. This is in consistent with CF versus n relationship observed in the earlier investigations (Ref 11-14).
5. H_d for base metal and its weldments increased with ε_{av} up to critical strain and thereafter decreased with further increase in strain due to the localization of plastic deformation, and this is in consistent with the literature data. Further, it was also observed that the onset of localization of plastic flow occurred early in weldments compared to its counterpart base metal.

6. The σ_d representing high strain rate (10^4 s^{-1}) flow stress of weldments and its base metal is about 1.5-1.7 times the value of flow stress under static loading conditions (10^{-3} s^{-1}) indicating the effect of strain rate. In addition, strain hardening of weldment-1 processed by LHF is superior to weldment-2 processed by ASS making the former candidate welding consumable for high strain rate applications.
7. The plastic flow behavior computed from DI is in good agreement with the data evaluated through SHPB experiments in the current study.

Acknowledgments

The authors are grateful to Vice Chancellor, DIAT (DU), Pune, for funding an internal project for design and development of high-velocity gas gun (HVGG) used for DI experiments in the present study. The authors are also thankful to Director, DMRL, Hyderabad, for providing Armox500T steel and extending experimental facilities for conducting a number of experiments. Acknowledgements are also due to scientists and technical staff of Amor division, Metal joining group, DMRL, Hyderabad.

References

1. Z. Xu and F. Huang, Plastic Behavior and Constitutive Modeling of Armor Steel Over Wide Temperature and Strain Rate Ranges, *Acta Mech. Solida Sin.*, 2012, **25**(6), p 598–608
2. G. Subhash, B.J. Koeppel, and A. Chandra, Dynamic Indentation Hardness and Rate Sensitivity in Metals, *J. Eng. Mater. Technol.*, 1999, **121**(3), p 257–263
3. C.H. Mok and J. Duffy, The Dynamic Stress–Strain Relation of Metals as Determined from Impact Tests with a Hard Ball, *Int. J. Mech. Sci.*, 1965, **7**(5), p 5367–6371
4. Y. Tirupataiah and G. Sundararajan, A Dynamic Indentation Technique for the Characterization of the High Strain Rate Plastic Flow Behavior of Ductile Metals and Alloys, *J. Mech. Phys. Solids*, 1991, **39**(2), p 243–271
5. G. Sundararajan and Y. Tirupataiah, The Localization of Plastic Flow Under Dynamic Indentation Conditions: I. Experimental Results, *Acta Mater.*, 2006, **54**(3), p 565–575
6. G. Sundararajan and Y. Tirupataiah, The Localization of Plastic Flow Under Dynamic Indentation Conditions: II. Analysis of Results, *Acta Mater.*, 2006, **54**(3), p 577–586
7. A. Kumaraswamy and V.V. Rao, High Strain-Rate Plastic Flow Behavior of Ti-6Al-4V from Dynamic Indentation Experiments, *Mater. Sci. Eng., A*, 2011, **528**(3), p 1238–1241
8. D. Tabor, A Simple Theory of Static and Dynamic Hardness, in *Proceedings of the Royal Society of London A: Mathematical, Physical and Engineering Sciences*, London 4 Feb 1948, vol. 192, No. 1029, pp. 247–274. The Royal Society
9. D. Tabor, *The Hardness of Metals*, Oxford University Press, Oxford, 2000
10. Y. Tirupataiah and G. Sundararajan, The Strain-Rate Sensitivity of Flow Stress and Strain-Hardening Rate in Metallic Materials, *Mater. Sci. Eng., A*, 1994, **189**(1–2), p 117–127
11. Y. Tirupataiah and G. Sundararajan, A Comprehensive Analysis of the Static Indentation Process, *Mater. Sci. Eng., A*, 1987, **91**, p 169–180
12. Y. Tirupataiah and G. Sundararajan, On the Constraint Factor Associated with the Indentation of Work-Hardening Materials with a Spherical Ball, *Metall. Trans. A*, 1991, **22**(10), p 2375–2384
13. A. Kumaraswamy and V.V. Rao, Effect of Temperature on Constraint Factor of IN718 Under Static Indentation Conditions, *Mater. Sci. Eng., A*, 2010, **527**(23), p 6230–6234
14. A. Kumaraswamy and B. Venkataraman, Effect of Temperature on Constraint Factor of Ti-6Al-4 V Under Static Indentation Conditions, *Scr. Mater.*, 2006, **54**(3), p 493–498
15. M.N.M. Patnaik, R. Narasimhan, and U. Ramamurty, Spherical Indentation Response of Metallic Glasses, *Acta Mater.*, 2004, **52**(11), p 3335–3345
16. H. Kolsky, An Investigation of the Mechanical Properties of Materials at Very High Rates of Loading, *Proc. Phys. Soc. London, Sect. B*, 1949, **62**(11), p 676
17. D. Mohr, G. Gary, and B. Lundberg, Evaluation of Stress–Strain Curve Estimates in Dynamic Experiments, *Int. J. Impact Eng*, 2010, **37**(2), p 161–169
18. C. Pandey, M.M. Mahapatra, P. Kumar, N. Saini, and A. Srivastava, Microstructure and Mechanical Property Relationship for Different Heat Treatment and Hydrogen Level in Multi-pass Welded P91 Steel Joint, *J. Manuf. Process.*, 2017, **28**, p 220–234
19. Q. Li, Y. Zhu, and J. Guo, Microstructure and Mechanical Properties of Resistance-Welded NiTi/Stainless Steel Joints, *J. Mater. Process. Technol.*, 2017, **249**, p 538–548
20. H. Alipooramirabad, A. Paradowska, R. Ghomashchi, and M. Reid, Investigating the Effects of Welding Process on Residual Stresses, Microstructure and Mechanical Properties in HSLA Steel Welds, *J. Manuf. Process.*, 2017, **28**, p 70–81
21. R. Pamnani, T. Jayakumar, M. Vasudevan, and T. Sakthivel, Investigations on the Impact Toughness of HSLA Steel Arc Welded Joints, *J. Manuf. Process.*, 2016, **21**, p 75–86
22. J. Verma and R.V. Taiwade, Dissimilar Welding Behavior of 22% Cr Series Stainless Steel with 316L and Its Corrosion Resistance in Modified Aggressive Environment, *J. Manuf. Process.*, 2016, **24**, p 1–10
23. R. Datta, D. Mukerjee, and S. Mishra, Weldability and Toughness Evaluation of Pressure Vessel Quality Steel using the Shielded Metal Arc Welding (SMAW) Process, *J. Mater. Eng. Perform.*, 1998, **7**(6), p 817–823
24. D. Shirmohammadi, M. Movahedi, and M. Pouranvari, Resistance Spot Welding of Martensitic Stainless Steel: Effect of Initial Base Metal Microstructure on Weld Microstructure and Mechanical Performance, *Mater. Sci. Eng., A*, 2017, **703**, p 154–161
25. I. Barényi, O. Híreš, and P. Lipták, Degradation of Mechanical Properties of Armored Steels After Its Welding, in *Proceedings of International Conference of Scientific Paper*, AFASES2011, 26-28 May 2011, Brasov, Romania, 2011, pp. 845–848
26. A. Grajcar, M. Morawiec, M. Różański, and S. Stano, Twin-Spot Laser Welding of Advanced High-Strength Multiphase Microstructure Steel, *Opt. Laser Technol.*, 2017, **92**, p 52–61
27. F. Sarsilmaz, I. Kirik, and S. Batı, Microstructure and Mechanical Properties of Armor 500/AISI2205 Steel Joint by Friction Welding, *J. Manuf. Process.*, 2017, **28**, p 131–136
28. A.L. Schaeffler, Constitution Diagram for Stainless-Steel Weld Metal. 2. Schaeffler Diagram, *Metal Progress*, 1974, **106**(1), p 227
29. P.B. Srinivasan, V. Muthupandi, V. Sivan, and W. Dietzel, Microstructure and Corrosion Behavior of Shielded Metal Arc-Welded Dissimilar Joints Comprising Duplex Stainless Steel and Low Alloy Steel, *J. Mater. Eng. Perform.*, 2006, **15**(6), p 758–764
30. R. Datta, D. Mukerjee, S. Jha, K. Narasimhan, and R. Veeraraghavan, Weldability Characteristics of Shielded Metal Arc Welded High Strength Quenched and Tempered Plates, *J. Mater. Eng. Perform.*, 2002, **11**(1), p 5–10